



## Dual mode luminescence from lanthanum orthovanadate nanoparticles

Tamilmani Vairapperumal<sup>a,\*</sup>, Mukhopadhyay Lakshmi<sup>b</sup>, Rai Vineet Kumar<sup>b</sup>,  
Sreeram Kalarical Janardhanan<sup>c</sup>, Mishra Ashok Kumar<sup>a</sup>

<sup>a</sup> Department of Chemistry, Indian Institute of Technology-Madras, Chennai, 600 036, Tamilnadu, India

<sup>b</sup> Laser and Spectroscopy Laboratory, Department of Applied Physics, Indian Institute of Technology (Indian School of Mines), Dhanbad, 826004, Jharkhand, India

<sup>c</sup> CLRI-CATERS, CSIR-Central Leather Research Institute, Chennai, 600020, Tamilnadu, India

### ABSTRACT

The structural and optical properties of Yb<sup>3+</sup>/Er<sup>3+</sup>/Eu<sup>3+</sup> co-doped LaVO<sub>4</sub> nanoparticles have been investigated by XRD, FT-IR, HRSEM, DRS and fluorescence analysis. The crystal structure of all the synthesized samples showed the existence of tetragonal LaVO<sub>4</sub>. Influence of Eu<sup>3+</sup> ions co-doping in Yb<sup>3+</sup>-Er<sup>3+</sup>:LaVO<sub>4</sub> nanoparticles are systemically studied for both upconversion luminescence and emission studies. The energy transfer mechanism involved in LaVO<sub>4</sub> phosphors is presented in detail based on their absorption, upconversion emission and pump power dependence study. The green to red fluorescence intensity ratio and asymmetry ratio are calculated with the variation of Eu<sup>3+</sup> ion concentration. The upconversion fluorescence intensity ratio increases with the increase of pump power density which attributes the application of present phosphors as temperature sensors. Color purity of Yb<sup>3+</sup>/Er<sup>3+</sup>/Eu<sup>3+</sup> co-doped LaVO<sub>4</sub> nanophosphors hardly shows any change with variations in pump power. Dual mode luminescence of these nanophosphors finds its applications in anti-counterfeiting inks.

### 1. Introduction

Rare earth ions doped phosphor material have achieved much attraction in the field of fingerprint detection, anti-counterfeiting and biological areas such as in-vivo bioimaging, therapy, drug delivery, sensing, and bio labeling applications, owing to their superior luminescence efficiency [1–8]. In these materials, luminescence takes place due to unique 4f-4f transition within ladder like energy levels present in the rare earth ions. The energy levels, shielded by the outer orbits [9], are insensitive to the host lattice environment and resemble that of free ions [10]. Lanthanide-doped phosphors are well known to exhibit not only conventional downconversion (DC) (i.e., Stokes shift) luminescence but also efficient upconversion (UC) (i.e., Anti-Stokes shift) luminescence [11–13]. In the nano regime, rare earth materials have been developed to be an efficient luminescent probe, unlike quantum dots for their indispensable role in energy transfer (ET) [14,15]. Several strategies can achieve a combination of down and upconversion luminescence in lanthanide nanoparticles (NPs) to obtain dual-mode luminescence: 1) Assembly of different luminescence components to form composite material, 2) Formation of UC/DC core/shell nanoparticles, 3) Combination of self-activated DC luminescence host and UC luminescence of rare earth ions, 4) UC and DC luminescence from the same activator in Yb<sup>3+</sup> co-doped system and 5) Direct approach through ternary lanthanide dopant system [16–21]. Multicolor emission from single host lattice makes them special for human mankind [22]. Appropriate selection of

host lattice plays a vital role in the luminescence efficiency of nano-crystalline materials. In search of suitable host lattice for upconversion luminescence, Lanthanide orthovanadate (LnVO<sub>4</sub>) is investigated to be an important class of rare earth inorganic compounds for their unique optical, chemical and electronic characteristics [23,24]. Among LnVO<sub>4</sub>, Lanthanum orthovanadate (LaVO<sub>4</sub>) generates impressive research for its polymorphic behavior. Generally, LaVO<sub>4</sub> can be crystallized either in Monazite-monoclinic (*m*-LaVO<sub>4</sub>) or zircon-tetragonal (*t*-LaVO<sub>4</sub>) crystal structure [25]. *t*-LaVO<sub>4</sub> is found to be a suitable host lattice, as it is thermodynamically metastable (i.e., less stable) when compared to *m*-LaVO<sub>4</sub> [26]. From the standpoint of material chemistry and luminescence, Eu<sup>3+</sup> doped tetragonal LaVO<sub>4</sub> represent fascinating models to improve fundamental ideas about their luminescence properties of doped systems [27–29]. Among the rare earth ions, Er<sup>3+</sup>, Tm<sup>3+</sup>, and Ho<sup>3+</sup> ions are familiar due to their upconversion luminescence and they are limited to multiplexing and multi-color applications for their microsecond lifetime and limited emission wavelength [30,31]. Eu<sup>3+</sup> ions show longer emission lifetime in millisecond range than that of Er<sup>3+</sup>, Tm<sup>3+</sup>, and Ho<sup>3+</sup> ions [32,33]. Only a few reports are focused on the UC emissions of Eu<sup>3+</sup> co-doped with Yb<sup>3+</sup> but not Eu<sup>3+</sup> alone due to the unmatched energy diagram and absence of intermediate energy level states [34]. Li et al., have recently studied the color tuning and dual-mode luminescence in BaGdF<sub>5</sub>:Yb<sup>3+</sup>, Er<sup>3+</sup>, Eu<sup>3+</sup> [35]. Using Yb<sup>3+</sup> and Er<sup>3+</sup> (Tm<sup>3+</sup>) ions as a double sensitizer, Eu<sup>3+</sup> doped fluoride nanostructures show unusual UC spectrum from visible to UV [36]. Xia

\* Corresponding author.

E-mail address: [tamilmani0512@gmail.com](mailto:tamilmani0512@gmail.com) (V. Tamilmani).

<https://doi.org/10.1016/j.jlumin.2019.116761>

Received 16 April 2019; Received in revised form 26 June 2019; Accepted 20 September 2019

Available online 20 September 2019

0022-2313/© 2019 Elsevier B.V. All rights reserved.

et al., have investigated the luminescence improvement by  $\text{Eu}^{3+}$  ions doping in  $\text{SrGdGa}_3\text{O}_7:\text{Yb}^{3+}, \text{Er}^{3+}, \text{Eu}^{3+}$  system [37]. There are no such reports to tune the upconversion emission using  $\text{Eu}^{3+}$  ions as a regulator in  $\text{LaVO}_4$  host lattice. Especially the energy transfer mechanism between  $\text{Er}^{3+}$  and  $\text{Eu}^{3+}$  ions have not been studied elaborately. There are no studies made on energy transfer between  $\text{Yb}^{3+}-\text{Er}^{3+}-\text{Eu}^{3+}$  ions in  $\text{LaVO}_4$  host lattice. What is worth noting,  $\text{LaVO}_4$  compound has been investigated only for upconversion emission in  $\text{Yb}^{3+}, \text{Er}^{3+}$  co-doped systems. Therefore, it is essential to study the behavior of activator dopant ions ( $\text{Eu}^{3+}$ ), to better understand both upconversion luminescence and emission process in  $\text{LaVO}_4$ .

Based on the literature, very low concentrations of  $\text{Yb}^{3+}$  and  $\text{Er}^{3+}$  ions are optimal for the upconversion emission [38]. The high dopants ion concentration increases the upconversion emission intensity, but also affects the host lattice crystal structure and may even induce the luminescence quenching [39]. In the present research work, we have employed the host lattice  $\text{LaVO}_4$  with 4 mol%  $\text{Yb}^{3+}$  ions and 2 mol %  $\text{Er}^{3+}$  ions, to investigate their luminescence, energy transfer mechanism on  $\text{Eu}^{3+}$  ion co-doping. In this study, we have primarily concentrated on the spectroscopic properties of  $\text{Yb}^{3+}/\text{Er}^{3+}/\text{Eu}^{3+}$  co-doped  $\text{LaVO}_4$  samples.

## 2. Experimental procedure

### 2.1. Synthesis of dual-mode luminescent nanoparticles (DLNPs)

Co-precipitation method followed by hydrothermal treatment is adopted for DLNPs synthesis. A mixture of  $\text{La}(\text{NO}_3)_3 \cdot 6\text{H}_2\text{O}$ ,  $\text{Yb}(\text{NO}_3)_3 \cdot 5\text{H}_2\text{O}$ ,  $\text{Er}(\text{NO}_3)_3 \cdot 5\text{H}_2\text{O}$  in 15 ml of double distilled water is added, such that the molar ratio of  $\text{La}^{3+}:\text{Yb}^{3+}:\text{Er}^{3+}$  remains constant as 1: 0.04: 0.02, respectively. To that, varying concentration of  $\text{Eu}(\text{NO}_3)_3 \cdot 5\text{H}_2\text{O}$  in 5 ml of double distilled water is added and stirred for 15 min to get a homogeneous solution (Molar ratio of  $\text{La}^{3+}$  to  $\text{Eu}^{3+}$  is maintained as 0, 0.01, 0.02, 0.03, 0.04, 0.05). Subsequently, 10 ml of  $\text{Na}_3\text{VO}_4$  is added dropwise to the above solution ( $\text{VO}_4^{3-}:\text{La}^{3+} = 1.05$ ) under stirring with the pH 9. Followed by 30 min of stirring, the as-obtained white colloidal dispersion is subjected to hydrothermal treatment at  $180^\circ\text{C}$  for 24 h. The resultant precipitate is separated by centrifugation, washed thrice with double distilled water and ethanol successively and then air-dried to get the white-colored solid.

The composition of dopants and sample name are presented in Table 1.

### 2.2. Methods

The X-ray diffractogram of all the synthesized  $\text{LaVO}_4$  nanoparticles are recorded at the scan rate of  $1^\circ \text{min}^{-1}$  in the  $2\theta$  range from  $10$  to  $80^\circ$  on a Bruker DA Advance X-ray diffractometer equipped with  $\text{Cu-K}\alpha$  radiation ( $\lambda = 1.540562 \text{ \AA}$ ). The GSAS-EXPGUI58 program is used for the Rietveld structure refinement from the powder XRD data. The refined parameters are scale factor, background as Chebyshev polynomial, unit cell parameters, profile function (Gaussian and Lorentzian parameters, sample displacement) and atomic positions. The initial structural models for all the doped  $\text{LaVO}_4$  nanoparticles are based on their single crystal X-

**Table 1**

Sample name and their corresponding dopants ion concentration for all doped/co-doped  $\text{LaVO}_4$  nanoparticles.

Sample name	Mol % of $\text{Yb}^{3+}$	Mol % of $\text{Er}^{3+}$	Mol % of $\text{Eu}^{3+}$
LV5U	–	–	5
LV4Y2E	4	2	–
LV4Y2E1U	4	2	1
LV4Y2E2U	4	2	2
LV4Y2E3U	4	2	3
LV4Y2E4U	4	2	4
LV4Y2E5U	4	2	5

ray structures. The single crystal X-ray structure of tetragonal  $\text{LaVO}_4$  is used as a structure model for all the doped  $\text{LaVO}_4$  nanoparticles. The structural models turned out to be the correct ones in all cases. For all atoms, the isotropic thermal parameters from the single crystal X-ray structure are used and not refined. Positional parameters and profile functions are refined in alternate cycles until no substantial changes are observed in the positional parameters. The structure refinement proceeded smoothly to yield acceptable agreement factors. The lattice parameters and cell volume are calculated from GSAS-EXPGUI58 program. The crystallite size calculated from the highest intensity peak of the prepared  $\text{LaVO}_4$  phosphor with the help of XRD peak broadening estimation using the Scherrer's formula ( $D = 0.89\lambda/\beta_f \cos\theta$ ), where 'D' is the crystallite size, ' $\lambda$ ' is the X-ray wavelength and ' $\theta$ ', ' $\beta_f$ ' is Bragg's angle and full width at half maximum (FWHM) of an estimated peak, respectively. The Williamson-Hall (W-H) plot is used to calculate the lattice strain present in the phosphor. The W-H plot is obtained from the equation  $\beta_f \cos\theta = 4\epsilon \sin\theta + (0.89\lambda/\beta_f \cos\theta)$ , where  $\epsilon$  is the strain present in the prepared  $\text{LaVO}_4$  phosphors. Lattice strain is calculated from the slope of a plot of  $\beta_f \cos\theta$  against  $4\sin\theta$ . Ionic radius percentage difference ( $D_r$ ) between dopant and substituted ions is calculated using the expression as  $D_r = R_s - R_d/R_s \times 100\%$ , where  $R_s$  and  $R_d$  are ionic radii (Coordination number = 8) of  $\text{La}^{3+}$  ions and  $\text{Yb}^{3+}, \text{Er}^{3+}$  and  $\text{Eu}^{3+}$  ions, respectively.

Morphology and size measurements of the doped  $\text{LaVO}_4$  nanoparticles are collected using a Hitachi S-4800 HRSEM operating at an accelerating voltage of 5 kV. Energy Dispersive X-ray Spectroscopy (EDX) measurements are carried out using a Quanta 200 FEG HRSEM operating at an accelerating voltage of 30 kV. FT-IR spectra are obtained using JASCO FT/IR 6300 spectrophotometer using the KBr pellet technique. UV-Visible absorption spectra are recorded using a Shimadzu UV-2600 spectrophotometer. UV-Vis-NIR diffuse reflectance spectra (DRS) are recorded in the absorbance mode at room temperature in the range of 400–1200 nm on Agilent technologies (CARY -5000) double-beam spectrophotometer equipped with integrating sphere attachment using  $\text{BaSO}_4$  as the reference. The instrument is interfaced with the computer for data collection and analysis. For these measurements, powder samples are filled in a hole of a sample holder, and the surface smoothed. Fluorescence spectra are recorded on a FluoroMax-4 spectrofluorometer using Xe flash lamp at room temperature. The asymmetric ratio is calculated as the relative emission intensity of electric dipole transition ( ${}^5\text{D}_0 \rightarrow {}^7\text{F}_2$ ) to the magnetic-dipole transition ( ${}^5\text{D}_0 \rightarrow {}^7\text{F}_1$ ). Luminescence decay curves are obtained from laser flash photolysis spectrometer (Spectra-Physics LAB 150). Samples were excited using Nd: YAG laser source at 266 nm (Fourth harmonics of a Nd: YAG laser). Absolute quantum yield by direct excitation method is calculated using the formula:  $\eta = \frac{E_s - E_R}{S_R - S_s}$ , where  $E_s, E_R$  are emission regions and  $S_s, S_R$  are scatter regions of the sample and reference, respectively. The UC emission spectra of the phosphor powders are recorded from 400 to 900 nm through a Princeton triple grating monochromator (Acton SP-2300) attached with a photomultiplier tube (PMT) upon excitation with 980 nm continuous wave (CW) diode laser. The upconversion is measured using the solid powder; the laser spot size is kept the same when comparing samples and the measurement spectra for all the samples are recorded under the same conditions. The position of the 980 nm laser relative to the samples is identical during all measurements and each sample is fixed on a metallic sample holder. Color analysis, i.e. CIE (Commission Internationale de L'Eclairage) is carried out using Color Calculator software. Dexter relation is used to study the type of interaction between the ions and are expressed as  $I(c) = \frac{C}{k \left(1 + \beta C^{\frac{2}{3}}\right)}$ , Where C = concentration of the dopant ions,  $I(c)$  = emission intensity corresponding to each dopant ion concentration, k and  $\beta$  are constants for each interaction condition.  $\left(-\frac{2}{3}\right)$  is the slope of  $\ln(I/C)$

versus  $\ln(C)$  and represents the interaction type between the dopant ions, Where  $\theta = 3, 6, 8, 10$  indicates exchange, dipole-dipole, dipole-quadrupole and quadrupole-quadrupole interaction between the activator ion species, respectively.

### 3. Results and discussion

#### 3.1. Structural analysis

Lanthanum orthovanadates ( $\text{LaVO}_4$ ) can be crystallized with monoclinic type-monazite or zircon type-tetragonal crystal structure. The diffraction peaks of all synthesized  $\text{LaVO}_4$  nanoparticles can be well-indexed to standard tetragonal  $\text{LaVO}_4$  phase (JCPDS No: 10-705226, space group:  $I_{41}/amd$  (141)), without any secondary phase as an impurity (Fig. 1). Tetragonal  $\text{LaVO}_4$  structure is composed of alternating edge sharing  $\text{LaO}_8$  dodecahedra and  $\text{VO}_4$  tetrahedra forming chains parallel to the c-axis. For each lanthanum or europium or vanadium center, there are four bond bridges of La/Eu-O-V with a maximum angle of  $153^\circ$  making the sigma bonding overlap efficiently and La/Eu occupies a high symmetry  $D_{2d}$  site environment.

The presence of broad and well-resolved diffraction peaks is a clear indication for nanocrystalline products. Ionic radii of  $\text{La}^{3+}$ ,  $\text{Yb}^{3+}$ ,  $\text{Er}^{3+}$  and  $\text{Eu}^{3+}$  with coordination number 8 are of 1.160, 0.985, 1.004 and 1.07 Å, respectively [40]. Radius percentage difference for  $\text{La}^{3+}/\text{Yb}^{3+}$ ,  $\text{La}^{3+}/\text{Er}^{3+}$ , and  $\text{La}^{3+}/\text{Eu}^{3+}$  are calculated as 15.1%, 13.5%, 7.8%, respectively and much smaller than 30%, representing that the dopants ions substitute the  $\text{La}^{3+}$  site in  $\text{LaVO}_4$  host lattice and in agreement with Vegard's law [41,42]. The average crystallite size of all synthesized NPs using Scherrer equation are found to be 15–50 nm [43–45]. Lattice strain (Supporting Information Fig. S1) induced by doping was evaluated using the Williamson-Hall (W-H) method [46], a very small value of tensile strain is noticed. Fig. 2 establishes the crystal structures of LV4Y2E5U and all the synthesized  $\text{LaVO}_4$  nanoparticles (Fig. S2) from Rietveld structural refinement of slow scan powder XRD data. Using

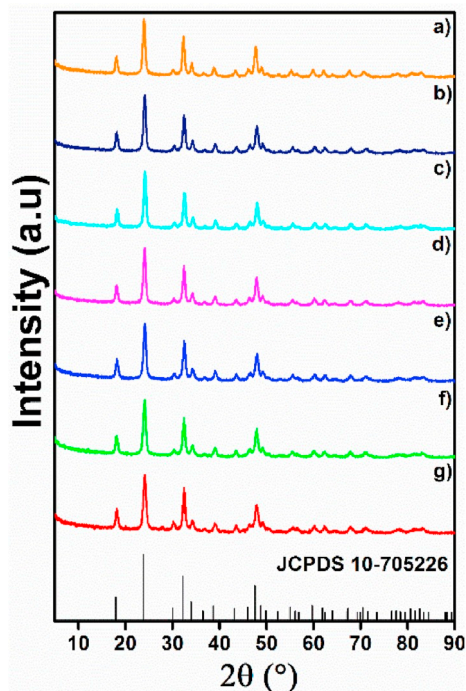


Fig. 1. XRD patterns of a) LV5U ( $\text{Eu}^{3+}:\text{Yb}^{3+}:\text{Er}^{3+} = 5:0:0$ ), b) LV4Y2E5U ( $\text{Eu}^{3+}:\text{Yb}^{3+}:\text{Er}^{3+} = 5:4:2$ ), c) LV4Y2E4U ( $\text{Eu}^{3+}:\text{Yb}^{3+}:\text{Er}^{3+} = 4:4:2$ ), d) LV4Y2E3U ( $\text{Eu}^{3+}:\text{Yb}^{3+}:\text{Er}^{3+} = 3:4:2$ ), e) LV4Y2E2U ( $\text{Eu}^{3+}:\text{Yb}^{3+}:\text{Er}^{3+} = 2:4:2$ ), f) LV4Y2E1U ( $\text{Eu}^{3+}:\text{Yb}^{3+}:\text{Er}^{3+} = 1:4:2$ ) and g) LV4Y2E ( $\text{Eu}^{3+}:\text{Yb}^{3+}:\text{Er}^{3+} = 0:4:2$ ). Standard tetragonal  $\text{LaVO}_4$  corresponds to JCPDS 10-705226.

Rietveld refinement procedure, we determined the lattice parameters and cell volume of all the  $\text{LaVO}_4$  NPs and are given in Table 2. Lattice parameters decrease with increasing  $\text{Eu}^{3+}$  concentration, indicates the efficient incorporation into the host lattice.

The surface morphology of all the synthesized  $\text{Yb}^{3+}/\text{Er}^{3+}/\text{Eu}^{3+}$  co-doped  $\text{LaVO}_4$  samples is studied using HRSEM images. LV4Y2E5U (Fig. 3a) are disclosed as homogeneous spherical nanoparticles with an average size ranging from 10 to 50 nm. The shape and size of nanoparticles are hardly changed with varying dopant ratio, which indicates that doping does not influence their morphology (Fig. S3). Energy dispersive X-ray (EDX) spectrum of LV4Y2E5U reveals the existence of La, V, O, Yb, Er, Eu and uniform distribution over the nanoparticles are presented in Fig. 3b and Supporting Information Fig. S4. Additionally, EDX spectra for LV5U and LV4Y2E are shown as Supporting Information Fig. S5.

In FT-IR spectra (Fig. S6), a strong absorption band at around  $797\text{ cm}^{-1}$  is assigned to the V–O bond vibration. The doublet peak around  $1420\text{ cm}^{-1}$  is due to the localized vibrations of the  $\text{VO}_4$  group present in the  $\text{LaVO}_4$  host lattice. Broad absorption bands around  $3300\text{ cm}^{-1}$  and  $1637\text{ cm}^{-1}$  are attributed to the O–H symmetric stretching and bending vibration of the adsorbed water molecules [7]. The spectra also show no significant difference between varying dopant ion concentration in the  $\text{LaVO}_4$  host lattice.

#### 3.2. Spectroscopic analysis

##### 3.2.1. Absorption study

The absorption spectra of all the prepared nanoparticles consist of a strong and broad absorption band at a shorter wavelength (274 nm) which attributes to the charge transfer (CT) transition from  $\text{VO}_4^{3-}$  groups to  $\text{Ln}^{3+}$  ions and are allowed by Laporte selection rules (Fig. 4 (i)) [47]. The f-f transitions of  $\text{Eu}^{3+}$  ions are not observed in the solution medium, owing to their forbidden transition. The UV–Vis–NIR absorption spectra of all the synthesized  $\text{LaVO}_4$  nanoparticles in the range of 200–1200 nm are measured against  $\text{BaSO}_4$  compound as a reference standard sample (Fig. 4 (ii)) and enlarged view in Fig. S7. Peak around 220 nm is attributed to the electronic transitions from O 2p valence band to La 5d 6s conduction band, i.e., host excitation. The broad and intense band around 250–350 nm is related to the overlapped CT bands, i.e.,  $\text{O}^{2-}$  to  $\text{La}^{3+}$  CT ( $\sim 260\text{ nm}$ , symmetry allowed) and  $\text{O}^{2-}$  to  $\text{V}^{5+}$  CT ( $\sim 340\text{ nm}$ , symmetry forbidden, within  $\text{VO}_4^{3-}$  groups) [24]. The weak and sharp peaks around 390 nm are due to  ${}^5\text{L}_6 \leftarrow {}^7\text{F}_0$  transition of  $\text{Eu}^{3+}$  ions [48].

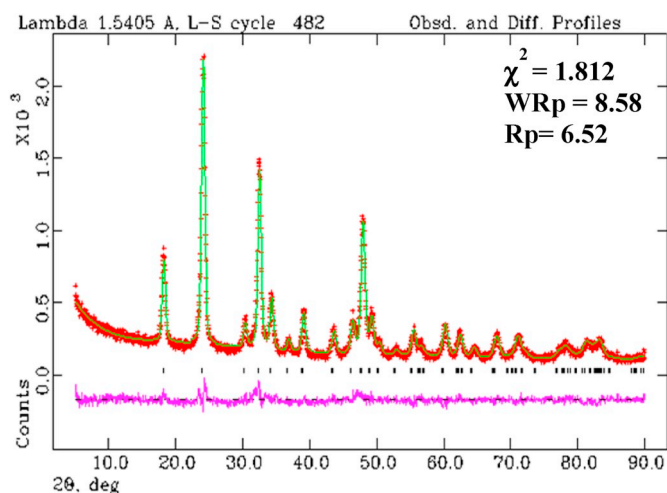


Fig. 2. Final Rietveld XRD plot of LV4Y2E5U ( $\text{Eu}^{3+}:\text{Yb}^{3+}:\text{Er}^{3+} = 5:4:2$ ) with the values of agreement factors and  $\chi^2$  (red, observed; green, calculated; black, vertical bars – positions of the Bragg reflections; pink, the difference between observed and calculated intensities).

**Table 2**

Summary of the lattice parameters, crystallite size and strain of doped LaVO<sub>4</sub> nanoparticles.

Sample Name	a = b (Å°)	c (Å°)	Cell Volume (Å°) <sup>3</sup>	Crystallite size (nm)	Strain
Standard Tetragonal 10705226	7.4578	6.5417	363.84		
LV5U	7.4568 (4)	6.5324 (6)	363.23(4)	20.72	0.00074
LV4Y2E	7.4499 (6)	6.5408 (8)	363.02(6)	29.99	0.00516
LV4Y2E1U	7.4533 (8)	6.5356 (12)	363.07(8)	53.61	0.00104
LV4Y2E2U	7.4526 (10)	6.5356 (15)	363.05(9)	22.65	0.0043
LV4Y2E3U	7.4550 (10)	6.5382 (15)	363.37(9)	19.21	0.00278
LV4Y2E4U	7.4499 (10)	6.5318 (16)	362.52 (10)	21.56	0.0043
LV4Y2E5U	7.4468 (8)	6.5305 (13)	362.15(8)	16.67	0.00194

With increasing Eu<sup>3+</sup> concentrations, CT bands shift towards the longer wavelength side and thus affects their shape. When only Eu<sup>3+</sup> is used as a dopant (LV5U), CT bands split thereby resulting the second CT band as maxima in comparison to the first transition. This is due to decrease in the symmetry of the VO<sub>4</sub><sup>3-</sup> groups and increased average distance between Eu<sup>3+</sup> ions and surrounding VO<sub>4</sub><sup>3-</sup>.

The absorption spectra exhibits eight absorption peaks at ~366 nm, ~379 nm, ~407 nm, ~490 nm, ~524 nm, ~545 nm, ~655 nm and ~802 nm are corresponding to the f-f electronic transitions from the ground state (G.S) <sup>4</sup>I<sub>15/2</sub> to <sup>4</sup>G<sub>9/2</sub>, <sup>4</sup>G<sub>11/2</sub>, <sup>2</sup>H<sub>9/2</sub>, <sup>4</sup>F<sub>7/2</sub>, <sup>2</sup>H<sub>11/2</sub>, <sup>4</sup>S<sub>3/2</sub>, <sup>4</sup>F<sub>9/2</sub> and <sup>4</sup>I<sub>9/2</sub> excited states of Er<sup>3+</sup> ions, respectively [49,50]. The broad absorption band at around 974 nm is due to large cross-section of Yb<sup>3+</sup> ions corresponding to the <sup>2</sup>F<sub>5/2</sub> ← <sup>2</sup>F<sub>7/2</sub> transition. The remaining very weak four absorption peaks are due to <sup>5</sup>L<sub>6</sub> ← <sup>7</sup>F<sub>0</sub> (~390 nm), <sup>5</sup>D<sub>3</sub> ← <sup>7</sup>F<sub>3</sub> (~444 nm), <sup>5</sup>D<sub>2</sub> ← <sup>7</sup>F<sub>0</sub> (~460 nm) and <sup>7</sup>F<sub>1</sub> ← <sup>5</sup>D<sub>1</sub> (~536 nm) transitions of Eu<sup>3+</sup> ions [51].

### 3.2.2. Effect of Eu<sup>3+</sup> doping on luminescence

**3.2.2.1. Emission study.** In Yb<sup>3+</sup>/Er<sup>3+</sup>/Eu<sup>3+</sup> co-doped LaVO<sub>4</sub> nanoparticles, there are two emitting ions (Er<sup>3+</sup>, Eu<sup>3+</sup>) and therefore their emissions are studied for both UV and NIR excitation. A series of Yb<sup>3+</sup>/Er<sup>3+</sup>/Eu<sup>3+</sup> co-doped LaVO<sub>4</sub> (Molar ratio of Eu<sup>3+</sup> = 0, 0.01, 0.02, 0.03, 0.04, 0.05) and Eu<sup>3+</sup> doped LaVO<sub>4</sub> (Molar ratio of Eu<sup>3+</sup> = 0.05) are

synthesized to investigate the influence of different Eu<sup>3+</sup> doping concentrations. The emission spectra (Fig. 5 (i)) obtained under UV irradiation (274 nm) is by the excitation of VO<sub>4</sub><sup>3-</sup> groups and energy level diagram is schematically presented in Supporting Information Fig. S8. Fig. 5i (a-f) shows the typical emissions of Eu<sup>3+</sup> ions in tetragonal LaVO<sub>4</sub>, which corresponds to f-f transitions of Eu<sup>3+</sup> ions. A weak emission band observed around 300–500 nm is due to vanadate lattice (Fig. 5i Inset) [26,52,53]. The broad emission band of VO<sub>4</sub><sup>3-</sup> (300–500 nm) overlaps with absorption bands of the Eu<sup>3+</sup> ion <sup>5</sup>L<sub>6</sub> ← <sup>7</sup>F<sub>0</sub> (~390 nm), <sup>5</sup>D<sub>3</sub> ← <sup>7</sup>F<sub>3</sub> (~444 nm), <sup>5</sup>D<sub>2</sub> ← <sup>7</sup>F<sub>0</sub> (~460 nm)). Fig. 5i (a-f) shows the variation in the emission intensities with a similar profile for different Eu<sup>3+</sup> concentrations.

The emission spectra of Yb<sup>3+</sup>/Er<sup>3+</sup>/Eu<sup>3+</sup> co-doped LaVO<sub>4</sub> nanoparticles emit an intense peak at ~618 nm corresponding to <sup>5</sup>D<sub>0</sub> → <sup>7</sup>F<sub>2</sub> transition, along with other emission peaks at ~593 nm, ~649 nm and ~697 nm which are due to the <sup>5</sup>D<sub>0</sub> → <sup>7</sup>F<sub>1</sub>, <sup>5</sup>D<sub>0</sub> → <sup>7</sup>F<sub>3</sub> and <sup>5</sup>D<sub>0</sub> → <sup>7</sup>F<sub>4</sub> transitions of Eu<sup>3+</sup> ions, respectively [54]. A weak band appears at ~536 nm corresponding to the <sup>5</sup>D<sub>1</sub> → <sup>7</sup>F<sub>1</sub> transition suggests that the cross relaxation between Eu<sup>3+</sup> ions and multiphonon relaxation in the <sup>5</sup>D<sub>1</sub> excited state are low [24]. The electric dipole transition (<sup>5</sup>D<sub>0</sub> → <sup>7</sup>F<sub>2</sub>) is hypersensitive in nature which is more intense than the magnetic dipole transition (<sup>5</sup>D<sub>0</sub> → <sup>7</sup>F<sub>1</sub>) attributing the occupation of Eu<sup>3+</sup> ions in D<sub>2d</sub> sites without an inversion center in tetragonal LaVO<sub>4</sub>. A very low intensity of the <sup>5</sup>D<sub>0</sub> → <sup>7</sup>F<sub>0</sub> transition at ~580 nm indicates its forbidden nature by Judd-Ofelt theory but observed due to J mixing effects. This discloses the presence of crystallographic non-equivalent sites of Eu<sup>3+</sup> ions in LaVO<sub>4</sub> host lattice. <sup>5</sup>D<sub>0</sub> → <sup>7</sup>F<sub>0</sub> transition also indicates that Eu<sup>3+</sup> ions are in a higher asymmetrical environment in LaVO<sub>4</sub> host lattice. The peak at 593 nm is due to the <sup>5</sup>D<sub>0</sub> → <sup>7</sup>F<sub>1</sub> magnetic-dipole transition, free from host matrix environment and Eu<sup>3+</sup> occupies a site with inversion center. The peak at 618 nm due to the <sup>5</sup>D<sub>0</sub> → <sup>7</sup>F<sub>2</sub> electric-dipole transition depends on the host lattice environment, forbidden by parity selection rules and Eu<sup>3+</sup> occupies a site without inversion center (low symmetry site). The ratio I(<sup>5</sup>D<sub>0</sub> → <sup>7</sup>F<sub>2</sub>)/I(<sup>5</sup>D<sub>0</sub> → <sup>7</sup>F<sub>1</sub>) 'known as asymmetry ratio' gives information about the coordination environment of Eu<sup>3+</sup> ions in the LaVO<sub>4</sub> host lattice. This ratio gives information about the occupation of Eu<sup>3+</sup> ions in higher or lower symmetry sites, degree of distortion from inversion symmetry of Eu<sup>3+</sup> ions surroundings in host lattice and color purity. High value of asymmetric ratio (>1) recommends that the Eu<sup>3+</sup> ions are located at high asymmetry sites of different valency and may form strong covalent bonds with the surroundings. In LaVO<sub>4</sub> host lattice, the value of asymmetric ratio obtained is 6.1 (> 1). This large value gives the measure of distortion degree from the inversion symmetry of Eu<sup>3+</sup> ions local environment in the LaVO<sub>4</sub> host lattice and hence leads to increase in red emission intensity (618 nm) [55].

With the increase in Eu<sup>3+</sup> concentration, the peak intensity increases

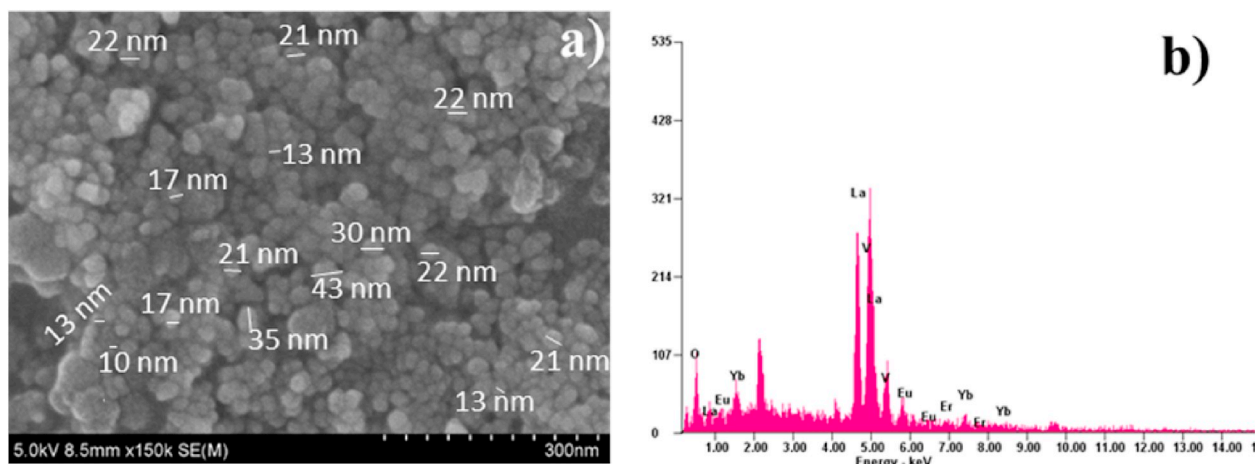


Fig. 3. HRSEM image a) and of LV4Y2E5U (Eu<sup>3+</sup>:Yb<sup>3+</sup>:Er<sup>3+</sup> = 5:4:2) and b) EDX spectrum of Yb<sup>3+</sup>/Er<sup>3+</sup>/Eu<sup>3+</sup> co-doped LaVO<sub>4</sub> nanoparticles.

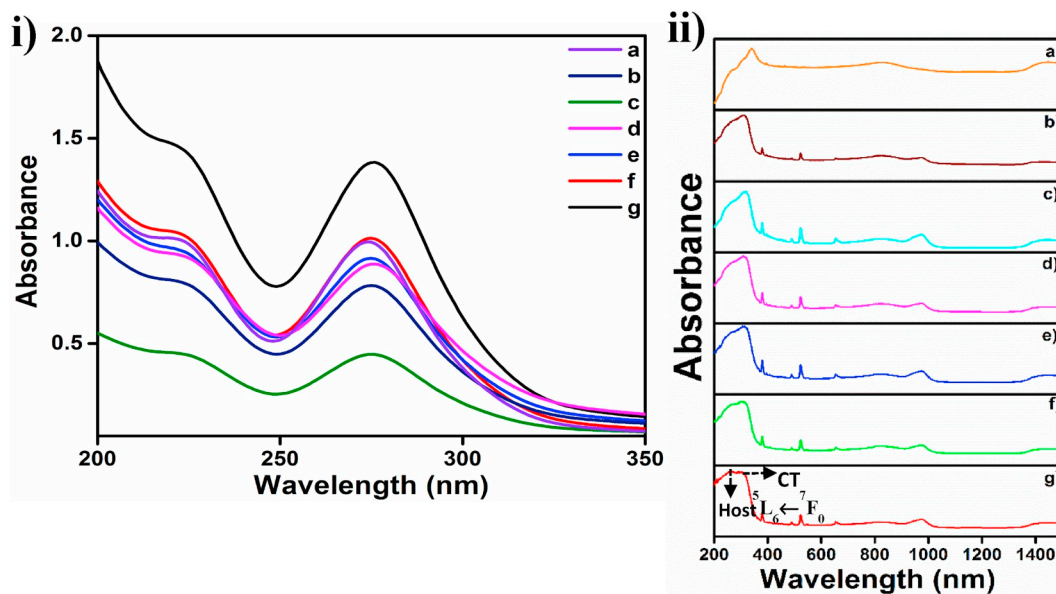


Fig. 4. Absorption (i) and DRS (ii) spectra of a) LV5U ( $\text{Eu}^{3+}:\text{Yb}^{3+}:\text{Er}^{3+} = 5:0:0$ ), b) LV4Y2E5U ( $\text{Eu}^{3+}:\text{Yb}^{3+}:\text{Er}^{3+} = 5:4:2$ ), c) LV4Y2E4U ( $\text{Eu}^{3+}:\text{Yb}^{3+}:\text{Er}^{3+} = 4:4:2$ ), d) LV4Y2E3U ( $\text{Eu}^{3+}:\text{Yb}^{3+}:\text{Er}^{3+} = 3:4:2$ ), e) LV4Y2E2U ( $\text{Eu}^{3+}:\text{Yb}^{3+}:\text{Er}^{3+} = 2:4:2$ ), f) LV4Y2E1U ( $\text{Eu}^{3+}:\text{Yb}^{3+}:\text{Er}^{3+} = 1:4:2$ ) and g) LV4Y2E ( $\text{Eu}^{3+}:\text{Yb}^{3+}:\text{Er}^{3+} = 0:4:2$ ).

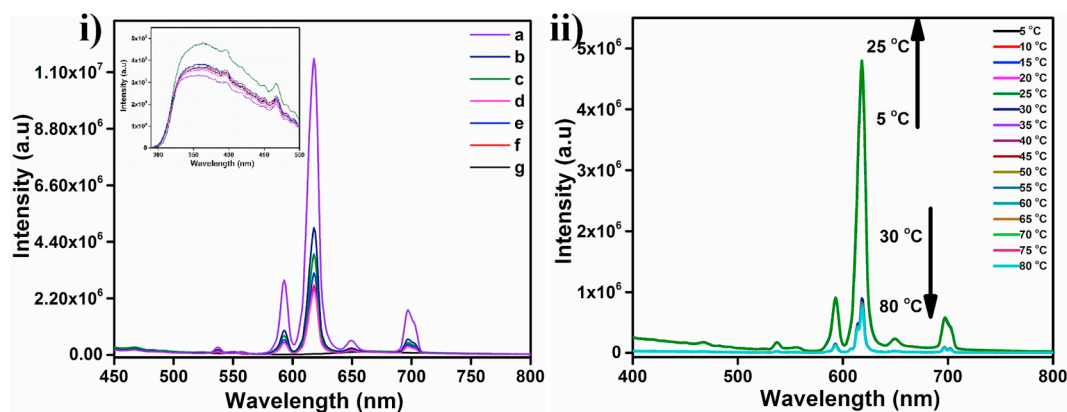


Fig. 5. (i) Emission spectra of a) LV5U ( $\text{Eu}^{3+}:\text{Yb}^{3+}:\text{Er}^{3+} = 5:0:0$ ), b) LV4Y2E5U ( $\text{Eu}^{3+}:\text{Yb}^{3+}:\text{Er}^{3+} = 5:4:2$ ), c) LV4Y2E4U ( $\text{Eu}^{3+}:\text{Yb}^{3+}:\text{Er}^{3+} = 4:4:2$ ), d) LV4Y2E3U ( $\text{Eu}^{3+}:\text{Yb}^{3+}:\text{Er}^{3+} = 3:4:2$ ), e) LV4Y2E2U ( $\text{Eu}^{3+}:\text{Yb}^{3+}:\text{Er}^{3+} = 2:4:2$ ), f) LV4Y2E1U ( $\text{Eu}^{3+}:\text{Yb}^{3+}:\text{Er}^{3+} = 1:4:2$ ) and g) LV4Y2E ( $\text{Eu}^{3+}:\text{Yb}^{3+}:\text{Er}^{3+} = 0:4:2$ ) at room temperature (Inset as emission from 300 to 500 nm) and (ii) Emission spectra of LV4Y2E5U ( $\text{Eu}^{3+}:\text{Yb}^{3+}:\text{Er}^{3+} = 5:4:2$ ) at different temperatures ( $\lambda_{\text{excitation}} = 274 \text{ nm}$ ).

and there is a direct consequence of  $\text{Eu}^{3+}$  concentration and distance between  $\text{Eu}^{3+}$  ions. This indicates that the  $\text{Eu}^{3+}$  ions do not undergo cross-relaxation process and therefore has high quenching concentration. The average distance (R) between  $\text{Eu}^{3+}$  ions can be calculated

according to the equation  $R = 2 \left( \frac{3V}{4\pi xN} \right)^{1/3}$ ; V= Unit cell volume,

x = Concentration of  $\text{Eu}^{3+}$  ions, N = Available number of crystallographic sites occupied by  $\text{Eu}^{3+}$  ions in the unit cell [56]. The corresponding R ( $\text{Eu}^{3+}:\text{Eu}^{3+}$ ) values are 2.588 nm (x = 0.01), 2.054 nm (x = 0.02), 1.795 nm (x = 0.03), 1.630 nm (x = 0.04) and 1.512 nm (x = 0.05) in  $\text{Yb}^{3+}/\text{Er}^{3+}/\text{Eu}^{3+}$  co-doped  $\text{LaVO}_4$  nanoparticles. This clearly establishes that the energy transfer between  $\text{Eu}^{3+}$  ions is strongly dependent on the average distance between  $\text{Eu}^{3+}$  ions. With the increase in  $\text{Eu}^{3+}$  concentration, R values decreases which in turn leads to increase in emission intensity and therefore energy migration cannot be omitted. Energy migration among  $\text{Eu}^{3+}$  ions in  $\text{Yb}^{3+}/\text{Er}^{3+}/\text{Eu}^{3+}$  co-doped  $\text{LaVO}_4$  nanoparticles may takes place in such a way that some of the excited  $\text{Eu}^{3+}$  ions return to ground state non-radiatively [57,58]. The strength of the resonance energy transfer between  $\text{Eu}^{3+}$  ions in  $\text{Yb}^{3+}/\text{Er}^{3+}/\text{Eu}^{3+}$  co-doped  $\text{LaVO}_4$  nanoparticles can be estimated by using Dexter

relation. The plot of  $\ln(I/C)$  versus  $\ln(C)$  (Supporting Information Fig. S9 (i)) gives the  $\theta$  value as 3. According to Van Uitert,  $\theta = 3$  corresponds to the energy transfer among nearest neighbor ions [59]. This indicates that the concentration quenching in  $\text{Yb}^{3+}/\text{Er}^{3+}/\text{Eu}^{3+}$  co-doped  $\text{LaVO}_4$  nanoparticles compared to LV5U, may be a consequence of exchange interaction between neighboring dopant ions.

Emission spectrum of LV4Y2E sample (Fig. 5g) consists four weak emission bands at  $\sim 490 \text{ nm}$ ,  $\sim 524 \text{ nm}$ ,  $\sim 545 \text{ nm}$  and  $\sim 655 \text{ nm}$  corresponding to the  ${}^4\text{F}_{7/2} \rightarrow {}^4\text{I}_{15/2}$ ,  ${}^2\text{H}_{11/2} \rightarrow {}^4\text{I}_{15/2}$ ,  ${}^4\text{S}_{3/2} \rightarrow {}^4\text{I}_{15/2}$  and  ${}^4\text{F}_{9/2} \rightarrow {}^4\text{I}_{15/2}$  transitions of  $\text{Er}^{3+}$  ion because under UV irradiation,  $\text{Yb}^{3+}$  ions cannot be excited. Under UV radiation, the vanadate groups transfer its energy to the activators ions ( $\text{Eu}^{3+}$  or  $\text{Er}^{3+}$ ), which then finally emit bright visible luminescence. Fig. 5 (i) establishes that in the  $\text{Yb}^{3+}/\text{Er}^{3+}/\text{Eu}^{3+}$  co-doped  $\text{LaVO}_4$  host lattice, energy transfer from  $\text{VO}_4^{3-}$  groups to  $\text{Eu}^{3+}$  ions is more efficient than that to the  $\text{Er}^{3+}$  ions [60]. Therefore, the optimum concentration for efficient emission process in  $\text{Yb}^{3+}/\text{Er}^{3+}/\text{Eu}^{3+}$  co-doped  $\text{LaVO}_4$  nanoparticles is 5 mol %  $\text{Eu}^{3+}$ . The emission spectra of LV4Y2E5U nanoparticles recorded at various temperatures ( $\lambda_{\text{ex}} = 274 \text{ nm}$ ) are shown in Fig. 5 (ii). With increase in temperature from 5 °C to 25 °C, the emission intensity enhances slightly but it decreases faster upon further increase in temperature from 30 °C

to 80 °C. This decrement in emission intensity at higher temperature is due to the thermal quenching phenomenon.  $\text{Eu}^{3+}$  ions show high vibronic transitions if the  $\text{Eu}^{3+}$  ion is at the centre of symmetry site. Therefore at a lower temperature, vibronic interactions are well conserved, resulting in strong increase of luminescence intensity. At high temperatures, quenching of fluorescence is ascribed to the thermally activated resonance crossovers from  ${}^5\text{D}_J$  state to CT states and then followed by return crossovers to a lower  ${}^5\text{D}_J$  states. The forced electric dipole  ${}^5\text{D}_0 \rightarrow {}^7\text{F}_4$  (697 nm) transition splits into 696 and 702 nm above 30 °C, indicates the possibility of at least two different local sites for  $\text{Eu}^{3+}$  ions, as it is sensitive to the local environment. This may be due to the impact of local crystal environment altered by the co-dopants at a higher temperature in LV4Y2E5U.

Fragments of the CIE chromaticity diagram with color coordinates of  $\text{Yb}^{3+}/\text{Er}^{3+}/\text{Eu}^{3+}$  co-doped  $\text{LaVO}_4$  nanoparticles as a function of  $\text{Eu}^{3+}$  concentration and  $\text{Eu}^{3+}$  co-doped  $\text{LaVO}_4$  nanoparticles are shown in Supporting Information Fig. S9 (ii). The color coordinates of undoped (LV4Y2E) and doped  $\text{Eu}^{3+}$  ions are located in the blue and orange-red region, respectively. With the variation of  $\text{Eu}^{3+}$  ion concentration, the CIE coordinate shifts from orange-red region towards the deeper red region and also close to the edge of the color diagram indicating the high color purity of the prepared samples. Thus,  $\text{Yb}^{3+}/\text{Er}^{3+}/\text{Eu}^{3+}$  co-doped  $\text{LaVO}_4$  nanoparticles may be suitable for color tunable display device applications.

The decay time behavior of  $\sim 618$  nm (Fig. 6),  $\sim 593$  nm and  $\sim 697$  nm (Fig. S10) emission bands for  $\text{Eu}^{3+}$  doped and  $\text{Yb}^{3+}/\text{Er}^{3+}/\text{Eu}^{3+}$  co-doped  $\text{LaVO}_4$  nanoparticles monitored at 266 nm excitation have been analyzed. Decay curves for all  $\text{Eu}^{3+}$  concentrations are

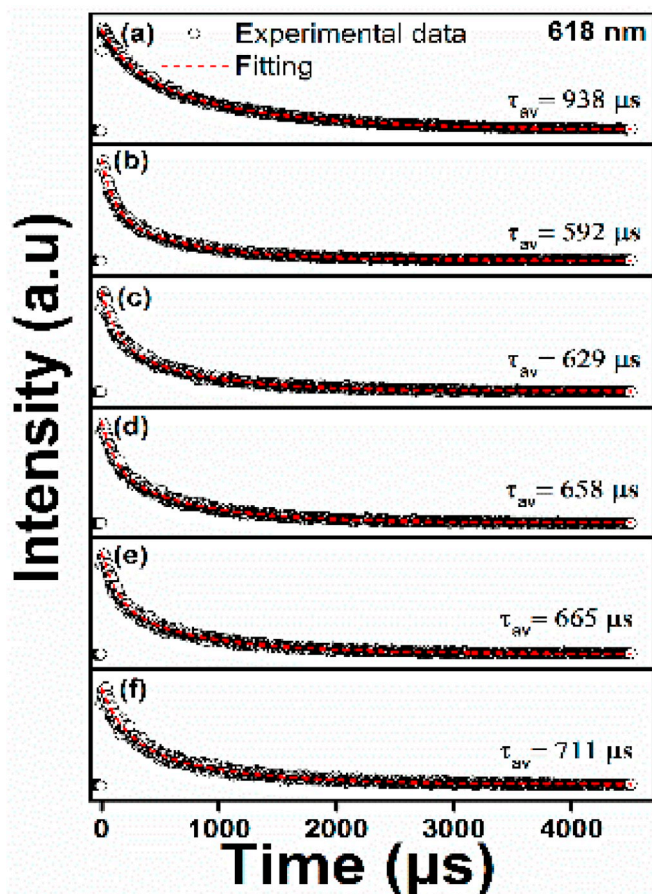


Fig. 6. Decay curves for the  $\text{Eu}^{3+}$  emission at 618 nm of a) LV5U ( $\text{Eu}^{3+}:\text{Yb}^{3+}:\text{Er}^{3+} = 5:0:0$ ), b) LV4Y2E5U ( $\text{Eu}^{3+}:\text{Yb}^{3+}:\text{Er}^{3+} = 5:4:2$ ), c) LV4Y2E4U ( $\text{Eu}^{3+}:\text{Yb}^{3+}:\text{Er}^{3+} = 4:4:2$ ), d) LV4Y2E3U ( $\text{Eu}^{3+}:\text{Yb}^{3+}:\text{Er}^{3+} = 3:4:2$ ), e) LV4Y2E2U ( $\text{Eu}^{3+}:\text{Yb}^{3+}:\text{Er}^{3+} = 2:4:2$ ) and f) LV4Y2E1U ( $\text{Eu}^{3+}:\text{Yb}^{3+}:\text{Er}^{3+} = 1:4:2$ ).

biexponential implying two different regions of co-doped  $\text{LaVO}_4$  nanoparticles like surface and bulk-related  $\text{Eu}^{3+}$  ions. All decay curves are fitted using double exponential decay function as  $I = I_0 + I_1 \exp(-t/\tau_1) + I_2 \exp(-t/\tau_2)$  [61]. This biexponential decay in microsecond-time range is due to spin and parity forbidden f-f transitions in  $\text{Yb}^{3+}/\text{Er}^{3+}/\text{Eu}^{3+}$  co-doped and  $\text{Eu}^{3+}$  doped  $\text{LaVO}_4$  nanoparticles. With increase in  $\text{Eu}^{3+}$  concentration, luminescence lifetime decreases which is attributed to an increase in the spontaneous emission transition probability. This indicates that shorter the emission lifetime, the stronger the emission intensity [29]. This phenomenon can be correlated to the decrease in the local symmetry of  $\text{Eu}^{3+}$  ions. Luminescence lifetime for 593 and 697 nm emission decreases with increase in  $\text{Eu}^{3+}$  concentration. Luminescence lifetime of  $\text{Eu}^{3+}$  ions oscillates between 0.94 and 0.54 ms, under 266 nm excitation and tabulated as Table S1.

Under 274 nm excitation, the absolute quantum yield of the developed  $\text{Yb}^{3+}/\text{Er}^{3+}/\text{Eu}^{3+}$  co-doped and  $\text{Eu}^{3+}$  doped  $\text{LaVO}_4$  nanoparticles are calculated to be 7–9%. Y. Zhydashchuk et al., explained the downconversion process in  $\text{Yb}^{3+}$  co-doped  $\text{Gd}_2\text{O}_3$  phosphors with a quantum yield (3–8%) and overall quantum efficiency (35%) by cooperative energy transfer [62].

**3.2.2.2. Upconversion study.** To investigate the upconversion mechanism of  $\text{Eu}^{3+}$  ions in  $\text{Yb}^{3+}/\text{Er}^{3+}$  doped  $\text{LaVO}_4$  nanoparticles, upconversion emission spectra (Fig. 7i) have been recorded in the range of 400–900 nm upon 980 nm continuous wave laser diode excitation. The frequency upconversion emission spectra of the  $\text{Yb}^{3+}/\text{Er}^{3+}:\text{LaVO}_4$  nanoparticles contains blue band at 490 nm, two dominant green emission bands at 524 nm and 545 nm, red band at 655 nm and NIR band at 802 nm corresponding to  ${}^4\text{F}_{7/2} \rightarrow {}^4\text{I}_{15/2}$ ,  ${}^2\text{H}_{11/2} \rightarrow {}^4\text{I}_{15/2}$ ,  ${}^4\text{S}_{3/2} \rightarrow {}^4\text{I}_{15/2}$ ,  ${}^4\text{F}_{9/2} \rightarrow {}^4\text{I}_{15/2}$  and  ${}^4\text{I}_{9/2} \rightarrow {}^4\text{I}_{15/2}$  transitions of  $\text{Er}^{3+}$  ion, respectively [63].

The upconversion peak positions remain unaltered with the incorporation of  $\text{Eu}^{3+}$  ions. In addition, with  $\text{Eu}^{3+}$  ions as a co-dopant in  $\text{Yb}^{3+}/\text{Er}^{3+}$  doped  $\text{LaVO}_4$  nanoparticles, a weak orange-red emission peak at approximately 618 nm corresponding to  ${}^5\text{D}_0 \rightarrow {}^7\text{F}_2$  transition of  $\text{Eu}^{3+}$  ions is observed.

It is clear that with the increment of  $\text{Eu}^{3+}$  ion concentration, the upconversion emission from  $\text{Er}^{3+}$  ions decreases (Fig. 7 (i)). With increasing  $\text{Eu}^{3+}$  ions concentration,  $\text{Eu}^{3+}$  ions tend to substitute  $\text{Er}^{3+}$  ions partly and reduce the energy transfer from the  $\text{Yb}^{3+}$  to  $\text{Er}^{3+}$  ions, which in turn increase the energy transfer to  $\text{Eu}^{3+}$  ions, resulting in the increase of  $\text{Eu}^{3+}$  and decrease of  $\text{Er}^{3+}$  emissions, simultaneously. It is found that the change in G/R ratio does not follow the trend with increasing  $\text{Eu}^{3+}$  concentration (Table 3), indicates that the decrease of green and red emissions is not gradual. This can be explained by the energy transfer mechanism in  $\text{Yb}^{3+}/\text{Er}^{3+}/\text{Eu}^{3+}$  co-doped  $\text{LaVO}_4$  nanoparticles. The intensity of upconversion emission bands in  $\text{Yb}^{3+}/\text{Er}^{3+}$  doped  $\text{LaVO}_4$  seems to be higher than that of  $\text{Yb}^{3+}/\text{Er}^{3+}/\text{Eu}^{3+}$  co-doped  $\text{LaVO}_4$  nanoparticles. The appearance of 618 nm band and the reduction of other emission peak intensity in the upconversion emission spectra of the  $\text{Yb}^{3+}/\text{Er}^{3+}/\text{Eu}^{3+}$  co-doped  $\text{LaVO}_4$  nanoparticles is due to the cross relaxation [ ${}^4\text{F}_{9/2}(\text{Er}^{3+}) + {}^7\text{F}_3(\text{Eu}^{3+}) \rightarrow {}^4\text{I}_{15/2}(\text{Er}^{3+}) + {}^5\text{D}_0(\text{Eu}^{3+})$ ] from  $\text{Er}^{3+}$  to  $\text{Eu}^{3+}$  ions [22].

In  $\text{Yb}^{3+}/\text{Er}^{3+}/\text{Eu}^{3+}$  co-doped  $\text{LaVO}_4$  nanoparticles, the dipole-dipole interaction ( $\theta = 6$ ) is responsible for the non-radiative energy transfer between the activator ions and hence the concentration quenching is obtained using Dexter's formula (Fig. 7 (ii)). The efficient green emission from  $\text{Yb}^{3+}/\text{Er}^{3+}/\text{Eu}^{3+}$  co-doped  $\text{LaVO}_4$  nanoparticles can be detected by the naked eye and is further confirmed by CIE color coordinates (As an inset in Fig. 7 (ii)).

To understand the possible upconversion mechanism the energy level diagram for the co-doped  $\text{LaVO}_4$  system is schematically presented in Fig. 8.

In  $\text{Yb}^{3+}/\text{Er}^{3+}:\text{LaVO}_4$  nanoparticles, at first  $\text{Yb}^{3+}$  ions absorb 980 nm radiation through ground state absorption (GSA) process and excited to

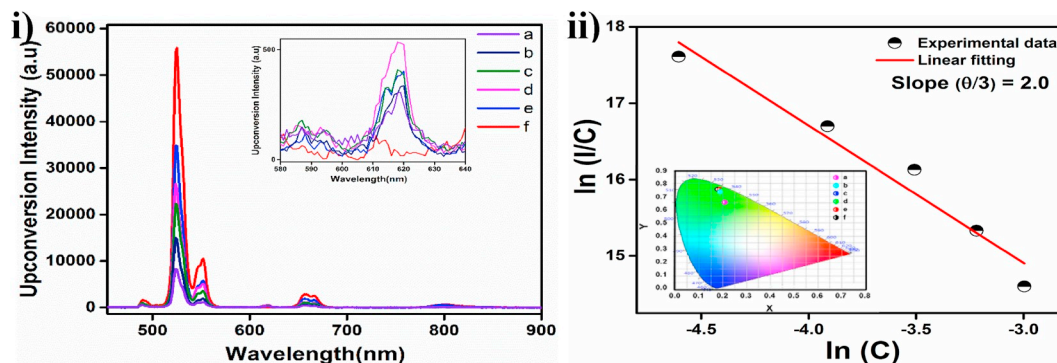


Fig. 7. (i) Upconversion spectra of a) LV4Y2E5U ( $\text{Eu}^{3+}:\text{Yb}^{3+}:\text{Er}^{3+} = 5:4:2$ ), b) LV4Y2E4U ( $\text{Eu}^{3+}:\text{Yb}^{3+}:\text{Er}^{3+} = 4:4:2$ ), c) LV4Y2E3U ( $\text{Eu}^{3+}:\text{Yb}^{3+}:\text{Er}^{3+} = 3:4:2$ ), d) LV4Y2E2U ( $\text{Eu}^{3+}:\text{Yb}^{3+}:\text{Er}^{3+} = 2:4:2$ ), e) LV4Y2E1U ( $\text{Eu}^{3+}:\text{Yb}^{3+}:\text{Er}^{3+} = 1:4:2$ ) and f) LV4Y2E ( $\text{Eu}^{3+}:\text{Yb}^{3+}:\text{Er}^{3+} = 0:4:2$ ) and (ii) Dexter plot of all the  $\text{Yb}^{3+}/\text{Er}^{3+}/\text{Eu}^{3+}$  co-doped  $\text{LaVO}_4$  nanoparticles. Enlarged view of 618 nm and CIE color coordinates as an inset in (i) and (ii), respectively. ( $\lambda_{\text{Excitation}} = 980 \text{ nm}$ ).

Table 3

Upconversion emission intensity and G/R ratio in doped  $\text{LaVO}_4$  nanoparticles.

Sample name	Green Integrated Intensity (G) (505–570 nm)	Red Integrated Intensity (R) (640–680 nm)	G/R ratio
LV4Y2E	767120	57294	13.39
LV4Y2E1U	446396	35890	12.44
LV4Y2E2U	357048	22866	15.61
LV4Y2E3U	304128	20841	14.59
LV4Y2E4U	182394	9963	18.31
LV4Y2E5U	109101	9752	11.19

$^2F_{5/2}$  level. The  $\text{Er}^{3+}$  ions are promoted to  $^4I_{11/2}$  level both from  $\text{Yb}^{3+}$  ions by energy transfer (ET-1) process as well as by GSA process from the ground state of  $\text{Er}^{3+}$  ions. After that, the excited state absorption (ESA-1) occurs from the  $^4I_{11/2}$  level and populates  $^4F_{7/2}$  level of  $\text{Er}^{3+}$  ions. The ET-2 process from  $\text{Yb}^{3+}$  to  $\text{Er}^{3+}$  ions also populates the  $^4F_{7/2}$  level. Non-radiative relaxation (NRR) process occurs from  $^4F_{7/2}$  level and then populates  $^2H_{11/2}$  and  $^4S_{3/2}$  energy levels of  $\text{Er}^{3+}$  ions. A part of the population in  $^4I_{11/2}$  energy level relaxes down to  $^4I_{13/2}$  level and then by ESA-2 process gets promoted to  $^4F_{9/2}$  level. Finally, the radiative emission occurs from  $^4F_{7/2}$ ,  $^2H_{11/2}$ ,  $^4S_{3/2}$  and  $^4F_{9/2}$  levels to the ground state  $^4I_{15/2}$ , resulting in peaks at 490 nm, 524 nm, 545 nm, and 655 nm, respectively. Some  $\text{Er}^{3+}$  ions from  $^4F_{9/2}$  level relax down non-radiatively to the  $^4I_{9/2}$  level and therefore  $^4I_{9/2} \rightarrow ^4I_{15/2}$  transition occurs resulting in 802 nm [64,65].

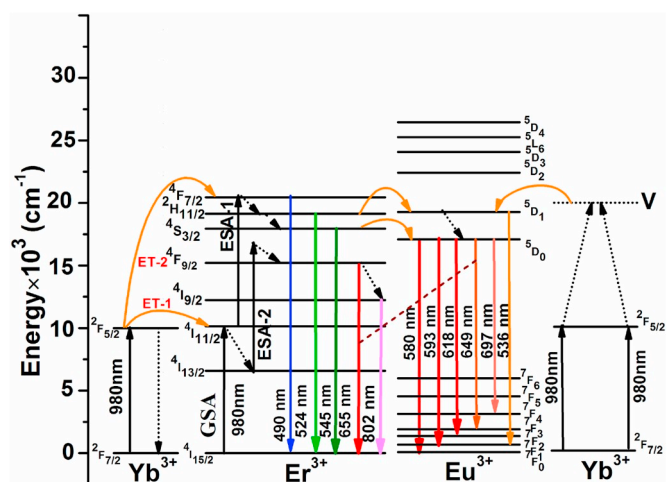


Fig. 8. Energy level diagram for  $\text{Yb}^{3+}-\text{Er}^{3+}-\text{Eu}^{3+}$  system in  $\text{LaVO}_4$  host lattice, representing the mechanism responsible for upconversion emission ( $V = \text{Virtual state}$ ).

In the case of  $\text{Yb}^{3+}/\text{Er}^{3+}/\text{Eu}^{3+}$  co-doped  $\text{LaVO}_4$  nanoparticles, large availability of  $\text{Er}^{3+}$  ions in  $^2H_{11/2}$  and  $^4S_{3/2}$  energy level enhances the probability of energy transfer from  $\text{Er}^{3+}$  ions to  $^5D_0$  energy level of  $\text{Eu}^{3+}$  ions. Thus, emission band corresponding to 618 nm of  $\text{Eu}^{3+}$  ions are amplified with increasing  $\text{Eu}^{3+}$  ions concentration. Other than the energy transfer from  $\text{Er}^{3+}$  to  $\text{Eu}^{3+}$  ions, the cooperative energy transfer from  $\text{Yb}^{3+}$  to  $\text{Eu}^{3+}$  ions is also responsible for increasing the intensity of the  $^5D_0 \rightarrow ^7F_2$  upconversion emission of  $\text{Eu}^{3+}$  ions. The cooperative energy transfer from  $\text{Yb}^{3+}$  to  $\text{Eu}^{3+}$  ions increases the population of  $^5D_1$  level. The multiphonon relaxation from the  $^4F_{7/2}$  and  $^5D_1$  level populates the  $^2H_{11/2}$ ,  $^4S_{3/2}$  and  $^5D_0$  levels and enhances the respective emission bands [66–69].

The photon number involved in the upconversion emission can be calculated from the slope value of double logarithmic plot between upconversion emission intensity and laser pump power (Fig. 9a). The relation between upconversion emission intensity ( $I_{\text{UC}}$ ) and pump power ( $P$ ) can be expressed by the equation  $I_{\text{UC}} \propto P^n$ , where  $n$  is the number of photons involved in the upconversion process [12]. Fig. 9a shows the  $\ln\text{-}\ln$  plots of upconversion emission on laser energy in  $\text{Yb}^{3+}/\text{Er}^{3+}/\text{Eu}^{3+}$  co-doped  $\text{LaVO}_4$  nanoparticles. The slope values indicate that  $^4I_{9/2} \rightarrow ^4I_{15/2}$  (802nm),  $^4F_{9/2} \rightarrow ^4I_{15/2}$  (655nm),  $^4S_{3/2} \rightarrow ^4I_{15/2}$  (545nm) and  $^4F_{7/2} \rightarrow ^4I_{15/2}$  (490 nm) transitions are due to two-photon absorption processes in  $\text{Yb}^{3+}/\text{Er}^{3+}/\text{Eu}^{3+}$  co-doped  $\text{LaVO}_4$  nanoparticles.

The upconversion emission intensity enhances with increase in pump power density for all the samples (Fig. 9b). With variation in the pump power density, the population of the  $^2H_{11/2}$  level increases more than that of the  $^4S_{3/2}$  level and thus the emission intensity of two green emission bands alter. Thus, the fluorescence intensity ratio (FIR) of two thermally coupled levels ( $\Delta E = \sim 735 \text{ cm}^{-1}$ ) increases, which follow a Boltzmann distribution of  $\text{Er}^{3+}$  ions ( $^2H_{11/2}$  &  $^4S_{3/2}$ ) [70]. With the increase in laser pump power density from  $7.01 \text{ W/cm}^2$  to  $75.9 \text{ W/cm}^2$ , the FIR of the samples LV4Y2E, LV4Y2E1U and LV4Y2E4U increases from 0.52 to 4.64, 0.39 to 3.69 and 1.09 to 3.85, respectively. At room temperature ( $T = 300 \text{ K}$ ), the sensor sensitivity for LV4Y2E, LV4Y2E1U and LV4Y2E4U samples is obtained as  $6.1 \times 10^{-3} \text{ K}^{-1}$ ,  $4.6 \times 10^{-3} \text{ K}^{-1}$  and  $12.8 \times 10^{-3} \text{ K}^{-1}$  respectively. In LV4Y2E, FIR variation is maximum because energy transfer occurs only from  $\text{Yb}^{3+}$  to  $\text{Er}^{3+}$  ions. In case of LV4Y2E1U and LV4Y2E4U samples, energy transfer occurs from the  $\text{Yb}^{3+}$  to both  $\text{Er}^{3+}$  and  $\text{Eu}^{3+}$  ions and also from  $\text{Er}^{3+}$  to  $\text{Eu}^{3+}$  ions. Thus, with the increase of  $\text{Eu}^{3+}$  ions concentration, the population of  $^2H_{11/2}$  and  $^4S_{3/2}$  levels decreases. As a result, different tendency of FIR variation is observed in all the samples.

#### 4. Conclusions

In summary, a series of tetragonal phased  $\text{LaVO}_4:\text{Yb}^{3+}/\text{Er}^{3+}$  nanoparticles with variable  $\text{Eu}^{3+}$  concentrations are prepared by co-precipitation technique followed by hydrothermal treatment at  $180^\circ \text{C}$

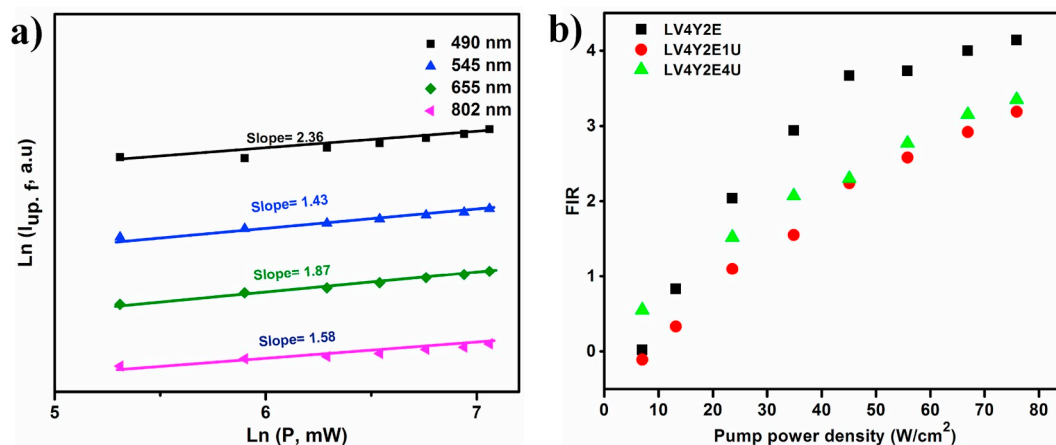


Fig. 9. Upconversion emission intensity (at different wavelengths) as a function of pump power for a) LV4Y2E1U ( $\text{Eu}^{3+}:\text{Yb}^{3+}:\text{Er}^{3+} = 1:4:2$ ) and b) corresponding FIR of doped  $\text{LaVO}_4$  nanoparticles.

for 24 h. On  $\text{Eu}^{3+}$  ions co-doping, the emission intensity of  $\text{Er}^{3+}$  ions decreases which confirms the energy transfer and cross relaxation processes between  $\text{Er}^{3+}$  and  $\text{Eu}^{3+}$  ions. The pump power dependence study shows that the upconversion FIR increases with the increase of laser pump power, which indicates that the developed  $\text{LaVO}_4$  phosphors may be used in temperature sensors. The developed nanophosphors exhibit intense green upconversion luminescence upon NIR radiation and red luminescence upon UV excitation. This dual-mode luminescence is a unique property of  $\text{LaVO}_4:\text{Yb}^{3+}/\text{Er}^{3+}/\text{Eu}^{3+}$  nanoparticles and develop as novel phosphors in anti-counterfeiting applications. Based on the experimental observations, it is concluded that the developed nanoparticles can be used in NIR to green upconverters, optical temperature sensors and color tunable display devices.

#### Acknowledgment

VT would like to thank the Science and Engineering (SERB) for the National Post-Doctoral Fellowship (NPDF).

#### Appendix A. Supplementary data

Supplementary data to this article can be found online at <https://doi.org/10.1016/j.jlum.2019.116761>.

#### References

- M. Wang, Y. Zhu, C. Mao, Synthesis of NIR-responsive  $\text{NaYF}_4:\text{Yb},\text{Er}$  upconversion fluorescent nanoparticles using an optimized solvothermal method and their applications in enhanced development of latent fingerprints on various smooth substrates, *Langmuir* 31 (2015) 7084–7090.
- J. Xu, L. Xu, C. Wang, R. Yang, Q. Zhuang, X. Han, Z. Dong, W. Zhu, R. Peng, Z. Liu, Near-Infrared-Triggered photodynamic therapy with multitasking upconversion nanoparticles in combination with checkpoint blockade for immunotherapy of colorectal cancer, *ACS Nano* 11 (2017) 4463–4474.
- M. Runowski, J. Marciniak, T. Grzyb, D. Przybylska, A. Shyichuk, B. Barszcz, A. Katrusiak, S. Lis, Lifetime nanomanometry - high-pressure luminescence of up-converting lanthanide nanocrystals -  $\text{SrF}_2:\text{Yb}^{3+},\text{Er}^{3+}$ , *Nanoscale* 9 (2017) 16030–16037.
- R. Deng, F. Qin, R. Chen, W. Huang, M. Hong, X. Liu, Temporal full-colour tuning through non-steady-state, upconversion 10 (2015) 237–242.
- M. An, J. Cui, Q. He, L. Wang, Down-/up-conversion luminescence nanocomposites for dual-modal cell imaging, *J. Mater. Chem. B* 1 (2013) 1333–1339.
- A. Zhou, F. Song, Y. Han, F. Song, D. Ju, X. Wang, Simultaneous size adjustment and upconversion luminescence enhancement of [small beta]- $\text{NaLuF}_4:\text{Yb}^{3+}/\text{Er}^{3+},\text{Er}^{3+}/\text{Tm}^{3+}$  microcrystals by introducing  $\text{Ca}^{2+}$  for temperature sensing, *CrystEngComm* 20 (2018) 2029–2035.
- T. Vairapperumal, D. Natarajan, K. Manikantan Syamala, S. Kalarical Janardhanan, N. Balachandran Unni, Catechin caged lanthanum orthovanadate nanorods for nuclear targeting and bioimaging applications, *Sens. Actuators B Chem.* 242 (2017) 700–709.
- T. Vairapperumal, A. Saraswathy, J.S. Ramapurath, S. Kalarical Janardhanan, N. Balachandran Unni, Catechin tuned magnetism of Gd-doped orthovanadate through morphology as T1-T2 MRI contrast agents, *Sci. Rep.* 6 (2016) 34976.
- G.B.a.B.C. Grabmaier, *Luminescent Materials*, Springer-Verlag Berlin Heidelberg, 1994.
- K. Binnemans, Lanthanide-based luminescent hybrid materials, *Chem. Rev.* 109 (2009) 4283–4374.
- F. Auzel, Upconversion and anti-Stokes processes with f and d ions in solids, *Chem. Rev.* 104 (2004) 139–174.
- V. Tamilmani, A.K. Soni, V.K. Rai, B.U. Nair, K.J. Sreeram, Frequency upconversion in catechin assisted  $\text{LaF}_3:\text{Yb}^{3+}+\text{Er}^{3+}$  square nanoplates, *J. Chem. Sci.* 129 (2017) 1929–1940.
- V. Tamilmani, B.U. Nair, K.J. Sreeram, Phosphate modulated luminescence in lanthanum vanadate nanorods- Catechin, polyphenolic ligand, *J. Solid State Chem.* 252 (2017) 158–168.
- D. Xu, C. Liu, J. Yan, S. Yang, Y. Zhang, Understanding energy transfer mechanisms for tunable emission of  $\text{Yb}^{3+}-\text{Er}^{3+}$  codoped  $\text{GdF}_3$  nanoparticles: concentration-dependent luminescence by near-infrared and violet excitation, *J. Phys. Chem. C* 119 (2015) 6852–6860.
- L. Woo, S. Roland, N. Kornelius, G. Ulrich, A template-based electrochemical method for the synthesis of multisegmented metallic nanotubes, *Angew. Chem. Int. Ed.* 44 (2005) 6050–6054.
- A.K. Singh, S.K. Singh, B.K. Gupta, R. Prakash, S.B. Rai, Probing a highly efficient dual mode: down-up-conversion luminescence and temperature sensing performance of rare-earth oxide phosphors, *Dalton Trans.* 42 (2013) 1065–1072.
- L. Peng, P. Qing, L. Yadong, Dual-mode luminescent colloidal spheres from monodisperse rare-earth fluoride nanocrystals, *Adv. Mater.* 21 (2009) 1945–1948.
- Y. Liu, K. Ai, L. Lu, Designing lanthanide-doped nanocrystals with both up- and down-conversion luminescence for anti-counterfeiting, *Nanoscale* 3 (2011) 4804–4810.
- P. Kumar, J. Dwivedi, B.K. Gupta, Highly luminescent dual mode rare-earth nanorod assisted multi-stage excitable security ink for anti-counterfeiting applications, *J. Mater. Chem. C* 2 (2014) 10468–10475.
- L. Wang, H. Chen, D. Zhang, D. Zhao, W. Qin, Dual-mode luminescence from lanthanide tri-doped  $\text{NaYF}_4$  nanocrystals, *Mater. Lett.* 65 (2011) 504–506.
- L. Yongsheng, T. Datao, Z. Haomiao, L. Renfu, L. Wenqin, C. Xueyuan, A strategy to achieve efficient dual-mode luminescence of  $\text{Eu}^{3+}$  in lanthanides doped multifunctional  $\text{NaGdF}_4$  nanocrystals, *Adv. Mater.* 22 (2010) 3266–3271.
- V.K. Rai, A. Pandey, R. Dey, Photoluminescence study of  $\text{Y}_2\text{O}_3:\text{Er}^{3+}-\text{Eu}^{3+}-\text{Yb}^{3+}$  phosphor for lighting and sensing applications, *J. Appl. Phys.* 113 (2013), 083104.
- M.N. Getz, P.-A. Hansen, O.S. Fjellvag, M.A.K. Ahmed, H. Fjellvag, O. Nilsen, Intense NIR emission in  $\text{YVO}_4:\text{Yb}^{3+}$  thin films by atomic layer deposition, *J. Mater. Chem. C* 5 (2017) 8572–8578.
- T. Grzyb, A. Szczeszak, A. Shyichuk, R.T. Moura, A.N.C. Neto, N. Andrzejewska, O. L. Malta, S. Lis, Comparative studies of structure, spectroscopic properties and intensity parameters of tetragonal rare earth vanadate nanophosphors doped with  $\text{Eu}(\text{III})$ , *J. Alloy. Comp.* 741 (2018) 459–472.
- V. Tamilmani, K.J. Sreeram, B.U. Nair, Tuned synthesis of doped rare-earth orthovanadates for enhanced luminescence, *RSC Adv.* 4 (2014) 4260–4268.
- R. Okram, N. Yaiphaba, R.S. Ningthoujam, N.R. Singh, Is higher ratio of monoclinic to tetragonal in  $\text{LaVO}_4$  a better luminescence host? Redispersion and polymer film formation, *Inorg. Chem.* 53 (2014) 7204–7213.
- Y. Zhu, Y. Ni, E. Sheng, Fluorescent  $\text{LaVO}_4:\text{Eu}^{3+}$  micro/nanocrystals: pH-tuned shape and phase evolution and investigation of the mechanism of detection of  $\text{Fe}^{3+}$  ions, *Dalton Trans.* 45 (2016) 8994–9000.
- C.K. Rastogi, S.K. Sharma, A. Patel, G. Parthasarathy, R.G.S. Pala, J. Kumar, S. Sivakumar, Dopant induced stabilization of metastable zircon-type tetragonal  $\text{LaVO}_4$ , *J. Phys. Chem. C* 121 (2017) 16501–16512.
- V. Tamilmani, K.J. Sreeram, B.U. Nair, Catechin assisted phase and shape selection for luminescent  $\text{LaVO}_4$  zircon, *RSC Adv.* 5 (2015) 82513–82523.

- [30] R. Lisiecki, E. Czyska, M. Żelechower, R. Swadźba, W. Ryba-Romanowski, Oxyfluoride silicate glasses and glass-ceramics doped with erbium and ytterbium - an examination of luminescence properties and up-conversion phenomena, *Mater. Des.* 126 (2017) 174–182.
- [31] Z. Xia, Y. Fu, T. Gu, Y. Li, H. Liu, Z. Ren, X. Li, G. Han, Fibrous CaF<sub>2</sub>:Yb,Er@SiO<sub>2</sub>-PAA 'tumor patch' with NIR-triggered and trackable DOX release, *Mater. Des.* 119 (2017) 85–92.
- [32] H. Dong, L.-D. Sun, W. Feng, Y. Gu, F. Li, C.-H. Yan, Versatile spectral and lifetime multiplexing nanoplatfrom with excitation orthogonalized upconversion luminescence, *ACS Nano* 11 (2017) 3289–3297.
- [33] Q. Ju, D. Tu, Y. Liu, R. Li, H. Zhu, J. Chen, Z. Chen, M. Huang, X. Chen, Amine-functionalized lanthanide-doped KGdF<sub>4</sub> nanocrystals as potential optical/magnetic multimodal bioprobes, *J. Am. Chem. Soc.* 134 (2012) 1323–1330.
- [34] Z. Leng, L. Li, D. Zhang, G. Li, Tunable green/red dual-mode luminescence via energy management in core-multishell nanoparticles, *Mater. Des.* 152 (2018) 119–128.
- [35] H. Li, G. Liu, J. Wang, X. Dong, W. Yu, Dual-mode, tunable color, enhanced upconversion luminescence and magnetism of multifunctional BaGdF<sub>5</sub>:Ln<sup>3+</sup> (Ln = Yb/Er/Eu) nanophosphors, *Phys. Chem. Phys.* 18 (2016) 21518–21526.
- [36] L. Wang, Z. Liu, Z. Chen, D. Zhao, G. Qin, W. Qin, Upconversion emissions from high-energy states of Eu<sup>3+</sup> sensitized by Yb<sup>3+</sup> and Ho<sup>3+</sup> in β-NaYF<sub>4</sub> microcrystals under 980 nm excitation, *Opt. Express* 19 (2011) 25471–25478.
- [37] H. Xia, J. Feng, Y. Ji, Y. Sun, Y. Wang, Z. Jia, C. Tu, 2.7 μm emission properties of Er<sup>3+</sup>/Yb<sup>3+</sup>/Eu<sup>3+</sup>: SrGdGa<sub>3</sub>O<sub>7</sub> and Er<sup>3+</sup>/Yb<sup>3+</sup>/Ho<sup>3+</sup>: SrGdGa<sub>3</sub>O<sub>7</sub> crystals, *J. Quant. Spectrosc. Radiat. Transf.* 173 (2016) 7–12.
- [38] V. Tamilmani, A. Kumari, V.K. Rai, B. Unni Nair, K.J. Sreeram, Bright green frequency upconversion in catechin based Yb<sup>3+</sup>/Er<sup>3+</sup> codoped LaVO<sub>4</sub> nanorods upon 980 nm excitation, *J. Phys. Chem. C* 121 (2017) 4505–4516.
- [39] L. Xing, W. Yang, J. Lin, M. Huang, Y. Xue, Enhanced and stable upconverted white-light emission in Ho<sup>3+</sup>/Yb<sup>3+</sup>/Tm<sup>3+</sup>-doped LiNbO<sub>3</sub> single crystal via Mg<sup>2+</sup> ion doping, *Sci. Rep.* 7 (2017) 14725.
- [40] R. Shannon, Revised effective ionic radii and systematic studies of interatomic distances in halides and chalcogenides, *Acta Crystallogr. A* 32 (1976) 751–767.
- [41] D. Peng, L. Laihui, Y.J. Su, Energy back transfer induced color controllable upconversion emissions in La<sub>2</sub>MoO<sub>6</sub>:Er<sup>3+</sup>/Yb<sup>3+</sup> nanocrystals for versatile applications, *Part. Part. Syst. Charact.* 35 (2018) 1700416.
- [42] K. Li, H. Lian, M. Shang, J. Lin, A novel greenish yellow-orange red Ba<sub>3</sub>Y<sub>4</sub>O<sub>9</sub>:Bi<sup>3+</sup>, Eu<sup>3+</sup> phosphor with efficient energy transfer for UV-LEDs, *Dalton Trans.* 44 (2015) 20542–20550.
- [43] U. Holzwarth, N. Gibson, The Scherrer equation versus the 'Debye-Scherrer equation', *Nat. Nanotechnol.* 6 (2011) 534.
- [44] H.P.A. Klug, L. E, in: *X-Ray Diffraction Procedures*, Wiley, 1974.
- [45] B.D. Cullity, *Elements of X-Ray Diffraction*, second ed., Addison-Wesley, 1978.
- [46] P.C. de Sousa Filho, T. Gacoin, J.-P. Boilot, R.I. Walton, O.A. Serra, Synthesis and luminescent properties of REVO<sub>4</sub>-REPO<sub>4</sub> (re = Y, Eu, Gd, Er, Tm, or Yb) heteronanostructures: a promising class of phosphors for excitation from NIR to VUV, *J. Phys. Chem. C* 119 (2015) 24062–24074.
- [47] G. Jia, Y. Song, M. Yang, Y. Huang, L. Zhang, H. You, Uniform YVO<sub>4</sub>:Ln<sup>3+</sup> (Ln=Eu, Dy, and Sm) nanocrystals: solvothermal synthesis and luminescence properties, *Opt. Mater.* 31 (2009) 1032–1037.
- [48] Z. Xu, C. Li, Z. Hou, C. Peng, J. Lin, Morphological control and luminescence properties of lanthanide orthovanadate LnVO<sub>4</sub> (Ln = La to Lu) nano-/microcrystals via hydrothermal process, *CrystEngComm* 13 (2011) 474–482.
- [49] C. Rennero-Lecuna, R. Martín-Rodríguez, R. Valiente, J. González, F. Rodríguez, K. W. Krämer, H.U. Güdel, Origin of the high upconversion green luminescence efficiency in α-NaYF<sub>4</sub>:2%Er<sup>3+</sup>,20%Yb<sup>3+</sup>, *Chem. Mater.* 23 (2011) 3442–3448.
- [50] M. Seshadri, E.F. Chillce, J.D. Marconi, F.A. Sigoli, Y.C. Ratnakaram, L.C. Barbosa, Optical characterization, infrared emission and visible up-conversion in Er<sup>3+</sup>-doped tellurite glasses, *J. Non-Cryst. Solids* 402 (2014) 141–148.
- [51] K. Binnemans, Interpretation of europium(III) spectra, *Coord. Chem. Rev.* 295 (2015) 1–45.
- [52] Y. Liusai, L. Guangshe, H. Wanbiao, Z. Minglei, S. Lang, Z. Jing, Y. Tingjiang, L. Liping, Control over the crystallinity and defect chemistry of YVO<sub>4</sub> nanocrystals for optimum photocatalytic property, *Eur. J. Inorg. Chem.* (2011) 2211–2220, 2011.
- [53] C. H. R.C. Powell, Energy transfer in europium doped yttrium vanadate crystals, *J. Lumin.* 10 (1975) 273–293.
- [54] Y.-C. Chang, C.-H. Liang, S.-A. Yan, Y.-S. Chang, Synthesis and photoluminescence characteristics of high color purity and brightness Li<sub>3</sub>Ba<sub>2</sub>Gd<sub>3</sub>(MoO<sub>4</sub>)<sub>8</sub>:Eu<sup>3+</sup> red phosphors, *J. Phys. Chem. C* 114 (2010) 3645–3652.
- [55] M. Janulevicius, P. Marmokas, M. Misevicius, J. Grigorjevaite, L. Mikoliunaite, S. Sakirzanovas, A. Katelnikovas, Luminescence and luminescence quenching of highly efficient Y<sub>2</sub>Mo<sub>4</sub>O<sub>15</sub>:Eu<sup>3+</sup> phosphors and ceramics, *Sci. Rep.* 6 (2016) 26098.
- [56] G. Blasse, Energy transfer in oxidic phosphors, *Phys. Lett. A* 28 (1968) 444–445.
- [57] G. Blasse, G.J. Dirksen, Long-range energy transfer from Gd<sup>3+</sup> to Pr<sup>3+</sup>, *J. Solid State Chem.* 73 (1988) 599–602.
- [58] G.-B. Xie, Luminescence and energy transfer in europium and bismuth codoped trisodium yttrium silicates, *Chin. Phys. Lett.* 30 (2013), 087802.
- [59] L.G. Van Uitert, Characterization of energy transfer interactions between rare earth ions, *J. Electrochem. Soc.* 114 (1967) 1048–1053.
- [60] V. Tamilmani, A. Kumari, V.K. Rai, B. Unni Nair, K.J. Sreeram, Bright green frequency upconversion in catechin based Yb<sup>3+</sup>/Er<sup>3+</sup> codoped LaVO<sub>4</sub> nanorods upon 980 nm excitation, *J. Phys. Chem. C* 121 (2017) 4505–4516.
- [61] Z. Zou, T. Wu, H. Lu, Y. Tu, S. Zhao, S. Xie, F. Han, S. Xu, Structure, luminescence and temperature sensing in rare earth doped glass ceramics containing NaY(WO<sub>4</sub>)<sub>2</sub> nanocrystals, *RSC Adv.* 8 (2018) 7679–7686.
- [62] Y. Zhdachevskyy, V. Tsiurma, M. Baran, L. Lipińska, P. Sybilski, A. Suchocki, Quantum efficiency of the down-conversion process in Bi<sup>3+</sup>-Yb<sup>3+</sup> co-doped Gd<sub>2</sub>O<sub>3</sub>, *J. Lumin.* 196 (2018) 169–173.
- [63] F. Zhang, G. Li, W. Zhang, Y.L. Yan, Phase-dependent enhancement of the green-emitting upconversion fluorescence in LaVO<sub>4</sub>:Yb<sup>3+</sup>, Er<sup>3+</sup>, *Inorg. Chem.* 54 (2015) 7325–7334.
- [64] M. Lin, Y. Zhao, M. Liu, M. Qiu, Y. Dong, Z. Duan, Y.H. Li, B. Pingguan-Murphy, T. J. Lu, F. Xu, Synthesis of upconversion NaYF<sub>4</sub>:Yb<sup>3+</sup>,Er<sup>3+</sup> particles with enhanced luminescent intensity through control of morphology and phase, *J. Mater. Chem. C* 2 (2014) 3671–3676.
- [65] L.F. Johnson, H.J. Guggenheim, T.C. Rich, F.W. Ostermayer, Infrared-to-Visible conversion by rare-earth ions in crystals, *J. Appl. Phys.* 43 (1972) 1125–1137.
- [66] G.S. Maciel, A. Biswas, P.N. Prasad, Infrared-to-visible Eu<sup>3+</sup> energy upconversion due to cooperative energy transfer from an Yb<sup>3+</sup> ion pair in a sol-gel processed multi-component silica glass, *Opt. Commun.* 178 (2000) 65–69.
- [67] F.Q. Renren Deng, Runfeng Chen, Wei Huang, Minghui Hong, Xiaogang Liu, Temporal full-colour tuning through non-steady-state upconversion, *Nat. Nanotechnol.* (2015).
- [68] A.P. Vineet Kumar Rai, Riya Dey, Photoluminescence study of Y<sub>2</sub>O<sub>3</sub>:Er<sup>3+</sup>+Eu<sup>3+</sup>+Yb<sup>3+</sup> phosphor for lighting and sensing applications, *J. Appl. Phys.* 113 (2013), 083104.
- [69] L. Mukhopadhyay, V.K. Rai, Investigation of photoluminescence properties, Judd-Ofelt analysis, luminescence nanothermometry and optical heating behaviour of Er<sup>3+</sup>/Eu<sup>3+</sup>/Yb<sup>3+</sup>:NaZnPO<sub>4</sub> nanophosphors, *New J. Chem.* 42 (2018) 13122–13134.
- [70] G. Gao, D. Busko, S. Kauffmann-Weiss, A. Turshatov, I.A. Howard, B.S. Richards, Wide-range non-contact fluorescence intensity ratio thermometer based on Yb<sup>3+</sup>/Nd<sup>3+</sup> co-doped La<sub>2</sub>O<sub>3</sub> microcrystals operating from 290 to 1230 K, *J. Mater. Chem. C* 6 (2018) 4163–4170.